PAPER

Check for updates

High throughput screening of novel tribromide perovskite materials for high-photovoltage solar cells†

Shi Chen, ‡[abc] Lihua Zhang,‡[bd] Yanliang Liu,‡[b] Zhuoqiong Zhang,[e] Yang Li,[b] Weizheng Cai,[b] Haiyan Lv,[b] Yanchun Qin,[b] Qianlong Liao,[b] Bin Zhou,[b] Ting Yan,[b] Jie Ren,[b] Shuming Chen, [f] Xiaodong Xiang,[b] Songyuan Dai, [g] Shu Kong So,[e] Xingzhu Wang,*[ab] Shihe Yang *[dh] and Baomin Xu *[b]

An efficient search for numerous novel mixed perovskite materials for high-performance solar cells leads to a strong demand for high throughput screening protocols. Highly efficient composition screening based on high throughput fabrication of discontinuous rather than compact perovskite films with comparable properties, which can save plenty of time and effort required for optimizing dense films and can significantly expand the applicability of the screening method to various perovskite compositions, has seldom been investigated. Especially, tribromide perovskites (~2.3 eV bandgap) with promising applications in tandem and spectral splitting devices require the efficient screening of new constituents to yield a high open-circuit voltage (V_{oc}). Herein, we develop a highly efficient composition screening protocol based on high throughput inkjet printing of discontinuous perovskite films with representative and comparable properties to accelerate the discovery of novel tribromide perovskites for high-photovoltage solar cells. 30 tribromide perovskite films with similar bandgaps are speedily and automatically inkjet-printed, and a very close grain size is acquired for all samples *via* optimizing the crystallization. Therefore, the corresponding photoluminescence (PL) lifetime database allows the efficient screening and identification of new constituents for high-photovoltage devices. To validate this, among the 30 samples, two compositions $(HC(NH_2)_2)_{0.4}(CH_3NH_3)_{0.6}PbBr_3$ ($FA_{0.4}MA_{0.6}$) and $(HC(NH_2)_2)_{0.1}(CH_3NH_3)_{0.9}PbBr_3$ ($FA_{0.1}MA_{0.9}$) with a long and short average PL lifetime, respectively, are screened out for device comparison. As expected, the $FA_{0.4}MA_{0.6}$ device delivers a high V_{oc} of 1.60 V with a champion efficiency of 9.25%, which is among the highest reported V_{oc} values for tribromide devices, much higher than that (1.45 V and 6.62%) of the $FA_{0.1}MA_{0.9}$ counterpart. Surprisingly, the V_{oc} limit for both devices is determined to be as high as 2.01 V for the first time. The V_{oc} and efficiency improvements principally result from the reduced trap states, lower level of energetic disorder, more efficient charge transport and decreased charge recombination losses. Additionally, the validity of the PL lifetime database is further confirmed by a high V_{oc} of 1.55 V obtained for another novel composition. These findings open up a new avenue for accelerated discovery of new perovskites for advanced device applications.

[a]Academy for Advanced Interdisciplinary Studies, Southern University of Science and Technology, Shenzhen, Guangdong Province 518055, China. E-mail: wangxz@sustech.edu.cn

[b]Department of Materials Science and Engineering, Shenzhen Engineering Research and Development Center for Flexible Solar Cells, Southern University of Science and Technology, Shenzhen, Guangdong Province 518055, China. E-mail: xubm@sustech.edu.cn

[c]Henan Key Laboratory of Photovoltaic Materials, Henan University, Kaifeng 475004, China

[d]Department of Chemistry, The Hong Kong University of Science and Technology, Clear Water Bay, Kowloon, Hong Kong, China

[e]Department of Physics, Hong Kong Baptist University, Kowloon Tong, Hong Kong, China

[f]Department of Electrical and Electronic Engineering, Southern University of Science and Technology, Shenzhen, Guangdong Province 518055, China

[g]State Key Laboratory of Alternate Electrical Power System with Renewable Energy Sources, North China Electric Power University, Beijing 102206, China

[h]Guangdong Key Lab of Nano-Micro Material Research, School of Chemical Biology and Biotechnology, Shenzhen Graduate School, Peking University, Shenzhen, Guangdong Province 518055, China. E-mail: chsyang@pku.edu.cn

† Electronic supplementary information (ESI) available. See DOI: 10.1039/d1ta06594g

‡ These authors contributed equally to this work.

1 Introduction

Hybrid organic–inorganic perovskites have been viewed as one of the most promising photovoltaic materials owing to their superior optoelectronic properties, and these materials are generally described with an ABX_3 formula, where A denotes monovalent cations (such as $CH_3NH_3^+$ (MA$^+$), $HC(NH_2)_2^+$ (FA$^+$), and Cs$^+$), B stands for divalent metal cations (namely Pb^{2+} and Sn^{2+}), and X represents halide anions (*i.e.* I$^-$, Br$^-$, and Cl$^-$).[1–3] Currently, the utilization of lead-based perovskites with multiple cations and hybrid halides as active layers in perovskite solar cells is emerging as a particularly effective approach to further improve device efficiency and stability.[4–8] Consequently, the combination of mixed multiple cations and hybrid halides generates a myriad of possible perovskite constituents. Such an enormous number of combinatorially available precursor compositions make the trial-and-error method time-consuming and inefficient, leading to a strong demand for high throughput synthesis. High throughput synthesis will permit the large-scale fabrication of perovskite films in a fast and reproducible manner, and the subsequent analysis regarding material properties will accelerate the discovery of novel perovskites for advanced device applications.

In this aspect, several research groups tried to develop a high throughput technique suitable for perovskite synthesis.[9–12] High throughput synthesis of perovskite single crystals and polycrystalline particles *via* a robot setup was demonstrated according to antisolvent crystallization.[9,10] However, the above prepared perovskites existed in the form of particles rather than thin films, and thus the corresponding property comparison cannot afford an effective and direct forecast of film-based device performance. Furthermore, 75 unique perovskite-inspired films were fabricated and characterized using an accelerated platform within 2 months.[11] This increased experimental throughput significantly accelerates the search for lead-free perovskites in the chemical space, but the preparation of dozens of perovskite films is still a major expenditure of time and the subsequent oversimplified property characterization (*i.e.* crystal phase and bandgap) cannot effectively identify the novel compositions for high-performance optoelectronic devices. Recently, our previous study developed a high throughput inkjet printing approach to fabricate 25 mixed perovskite films in 10 minutes, and the subsequently obtained bandgaps and PL lifetimes of these films allowed the accelerated screening of perovskite constituents for photovoltaic applications.[12] Apparently, this type of composition screening based on high throughput inkjet printing is very useful for the discovery of novel perovskites, but the pre-printing adjustment and optimization for acquiring high-quality perovskite films are very time-consuming, and besides it is difficult to adopt this high throughput printing technique to produce continuous and compact perovskite films for some compositions due to their significantly different crystallization dynamics. Therefore, for a more efficient search for novel perovskite materials, high throughput composition screening based on discontinuous rather than compact perovskite films with representative and comparable properties needs to be urgently developed, which can save a great deal of time and effort required for inkjet printing dense films and can further expand the applicability of our screening protocol to various perovskite compositions.

A variety of perovskite film deposition technologies, including spin coating,[5,13] blade coating,[14–17] thermal evaporation,[2] spray deposition[18,19] and inkjet printing,[20–23] have been exploited. Among these techniques, inkjet printing has been considered as an extremely promising method to manufacture perovskite films in a high throughput way due to its *in situ* mixing capability, low material consumption and high writing accuracy. Over the past few years, the crystallization process of inkjet-printed perovskite films was extensively explored and optimized, and the corresponding solar cells demonstrated a continuous power conversion efficiency (PCE) increase to 21.6%.[22–25] Despite significant advances toward high-quality inkjet-printed films, most research efforts were concentrated on inkjet printing single-component perovskite films rather than multi-component perovskite films in a batch. The remarkably increased control complexity in the printing details and the crystallization dynamics largely hinders the development of inkjet printing multi-component perovskite films. Lately, our research work demonstrated 25 mixed perovskite films which were inkjet-printed in 10 minutes in a batch by *in situ* mixing four inks from separate ink cartridges,[12] but the pre-printing parameter optimization for obtaining continuous and compact films took a huge amount of time, which substantially lowered the time efficiency of perovskite composition screening and identification. To date, the highly efficient composition screening based on high throughput inkjet printing of multi-component perovskite films still remains a daunting challenge.

Tribromide perovskites with a bandgap of ∼2.3 eV have great potential to yield a high V_{oc}, which makes these materials promising for applications in tandem solar cells and driving electrochemical reactions.[26–28] Significant efforts were undertaken to optimize and enhance the V_{oc} of perovskite devices.[29–31] At the early stage, engineering advanced hole and electron transport layers gave rise to a high V_{oc} of approximately 1.5 V in both MAPbBr$_3$ and FAPbBr$_3$ solar cells.[32–35] Moreover, tailoring the crystallization process and optimizing the precursor solvent also enabled MAPbBr$_3$ devices to yield a V_{oc} beyond 1.5 V.[36,37] Meanwhile, the employment of carbon electrodes further pushed the V_{oc} of MAPbBr$_3$ and CsPbBr$_3$ devices to a higher level (close to 1.6 V).[38,39] In addition, a record V_{oc} exceeding 1.6 V in the MAPbBr$_3$ stack was realized by inserting anode and cathode interfacial modification layers.[40] In spite of significant progress toward a high V_{oc} for tribromide perovskite devices, the adopted active layer materials in these studies are restricted to three most common constituents (MAPbBr$_3$, FAPbBr$_3$ and CsPbBr$_3$) rather than new perovskite compositions since the fabrication of high-quality mixed tribromide perovskite films and the subsequent effective composition screening require considerable research time and effort. The exploration of new tribromide perovskite compositions can not only considerably enlarge the diversity of tribromide perovskites but also greatly

promote the rapid development of optoelectronic devices based on these novel materials. More importantly, it is well known that the compositional engineering of triiodide perovskites normally produces a higher V_{oc} and better device performance.[1] As a consequence, novel tribromide perovskite materials with different compositions need to be urgently exploited and developed to investigate the attainable V_{oc}.

Given these considerations, a highly efficient composition screening protocol based on high throughput inkjet printing of discontinuous rather than compact perovskite films with representative and comparable properties is developed to accelerate the discovery of novel tribromide perovskite materials for high-photovoltage solar cells. To be specific, the sequential inkjet printing of three precursor solutions results in the formation of 30 mixed tribromide perovskite films with similar bandgaps in a fast and automated manner, and all films have a very close grain size *via* optimizing the crystallization kinetics. As a result, the obtained PL lifetime database for the 30 mixed films allows us to efficiently screen and identify novel compositions for high-photovoltage solar cells. In order to verify this concept, two compositions of $FA_{0.4}MA_{0.6}$ and $FA_{0.1}MA_{0.9}$ have a long (32.36 ns) and short (0.57 ns) average PL lifetime, respectively, and thereby are screened out from the 30 tested films for device investigations. The $FA_{0.4}MA_{0.6}$ device exhibits an optimal PCE of 9.25% along with a high V_{oc} of 1.60 V, which is among the highest reported V_{oc} values for tribromide perovskite solar cells. As expected, these photovoltaic parameters for the $FA_{0.4}MA_{0.6}$ device are much better than those (6.62% and 1.45 V) for the $FA_{0.1}MA_{0.9}$ counterpart. The superior device performance is primarily explained by the reduced trap states, lower level of energetic disorder and more efficient charge transport as well as considerably decreased charge recombination losses. Besides, another novel composition of $(FA)_{0.9}(MA)_{0.1}PbBr_3$ ($FA_{0.9}MA_{0.1}$) with a long average PL lifetime also delivers a high V_{oc} of 1.55 V, further confirming the validity of the PL lifetime database. This work affords an efficient route to accelerate the discovery of novel perovskite materials for advanced applications.

2 Results and discussion

In order to accelerate the discovery of novel perovskite materials for advanced device applications, we propose a highly efficient composition screening protocol based on high throughput inkjet printing, as presented in Fig. 1. In the following, we use an accelerated discovery of novel tribromide perovskites for high-photovoltage devices as an experimental proof of concept for our screening protocol.

We developed an inkjet printing technique for high throughput manufacture of compact mixed perovskite films in our recent work.[12] In order to realize the high throughput synthesis of discontinuous perovskite films with comparable and representative properties, this inkjet printing approach is greatly updated in this work and the corresponding working principle is briefly described below. Fig. 2a illustrates the schematic diagram of the four-channel non-parallel drop-on-demand (DOD) inkjet printer (the photograph in Fig. S2†) including four printheads, four ink cartridges, a mobile flat plate and a programmable control system. During the jetting process, the programmable control system can precisely control the ejected single droplet volume, the droplet number and the location of printed dots as well as the printing sequence of precursors. As depicted in Fig. 2b, except an empty one, three ink cartridges are filled with $FAPbBr_3$, $MAPbBr_3$ and $CsPbBr_3$ precursor solutions, respectively, and the corresponding printheads eject the precursor droplets onto glass substrates in sequence to form mixed precursor films before annealing. It should be pointed out that the whole printing process for mixed perovskite films is fully automated. When we fix the total ejected dots (37 500) for each mixed film and the jetted single droplet volume (100 pL), the composition of mixed perovskite films is principally determined by the ejected droplet number from each printhead. To demonstrate the impressive control over printing details, a series of $FAPbBr_3$ films are inkjet-printed with decreased ejected dots from left to right, and the resulting film colour gradually changes from dark yellow to light yellow (Fig. 2c). Furthermore, the printing of irregular shaped symbols
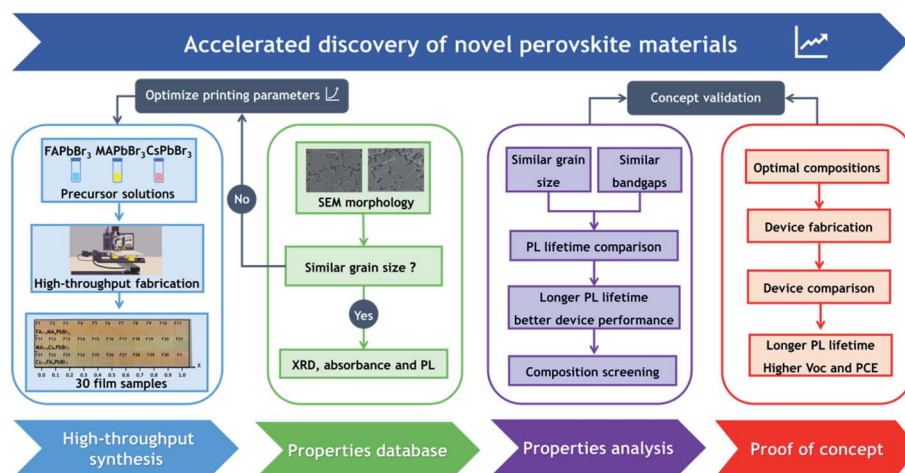

Fig. 1 A framework of our proposed composition screening protocol based on high throughput synthesis.
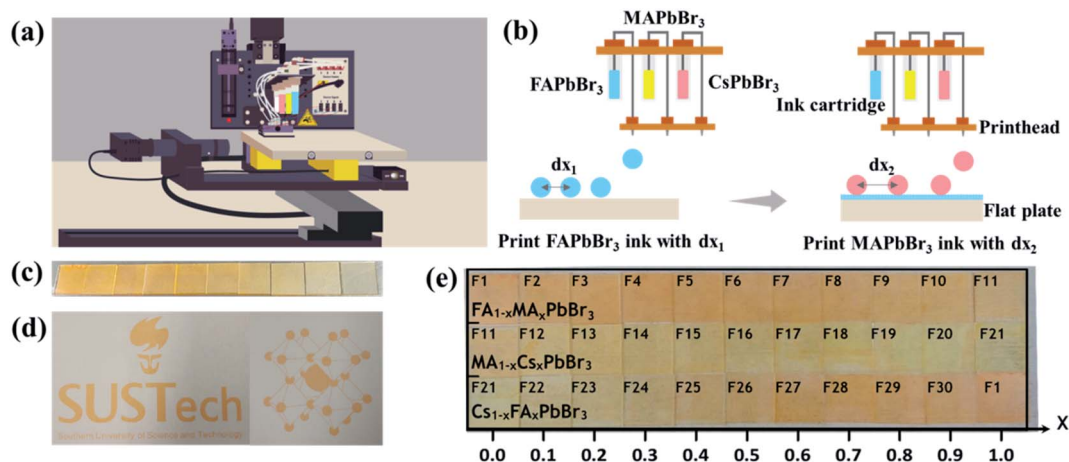
Fig. 2 (a) Schematic diagram of the four-channel non-parallel drop-on-demand (DOD) inkjet printer. (b) Schematic diagram of the fabrication of mixed perovskite films ($FA_{1-x}MA_xPbBr_3$, $MA_{1-x}Cs_xPbBr_3$ or $Cs_{1-x}FA_xPbBr_3$), where the sequential printing of two different precursors with various volume ratios yields a series of mixed films. (c) Inkjet-printed $FAPbBr_3$ films with decreased ejected dots from left to right. (d) The inkjet-printed school logo (left) and perovskite crystal structure (right). (e) Inkjet-printed $FA_{1-x}MA_xPbBr_3$, $MA_{1-x}Cs_xPbBr_3$ and $Cs_{1-x}FA_xPbBr_3$ films marked with numbers from 1 to 30.

such as the school logo and the perovskite crystal structure is also achievable, as displayed in Fig. 2d.

As shown in Fig. 2e, any two of $FAPbBr_3$, $MAPbBr_3$ and $CsPbBr_3$ precursors are sequentially printed on glass substrates with mixing ratios between 0% and 100% in 10% steps, producing 30 mixed perovskite films. The as-fabricated films are marked with numbers from 1 to 30 for simplicity. Strikingly, the whole printing process of 30 mixed films was highly
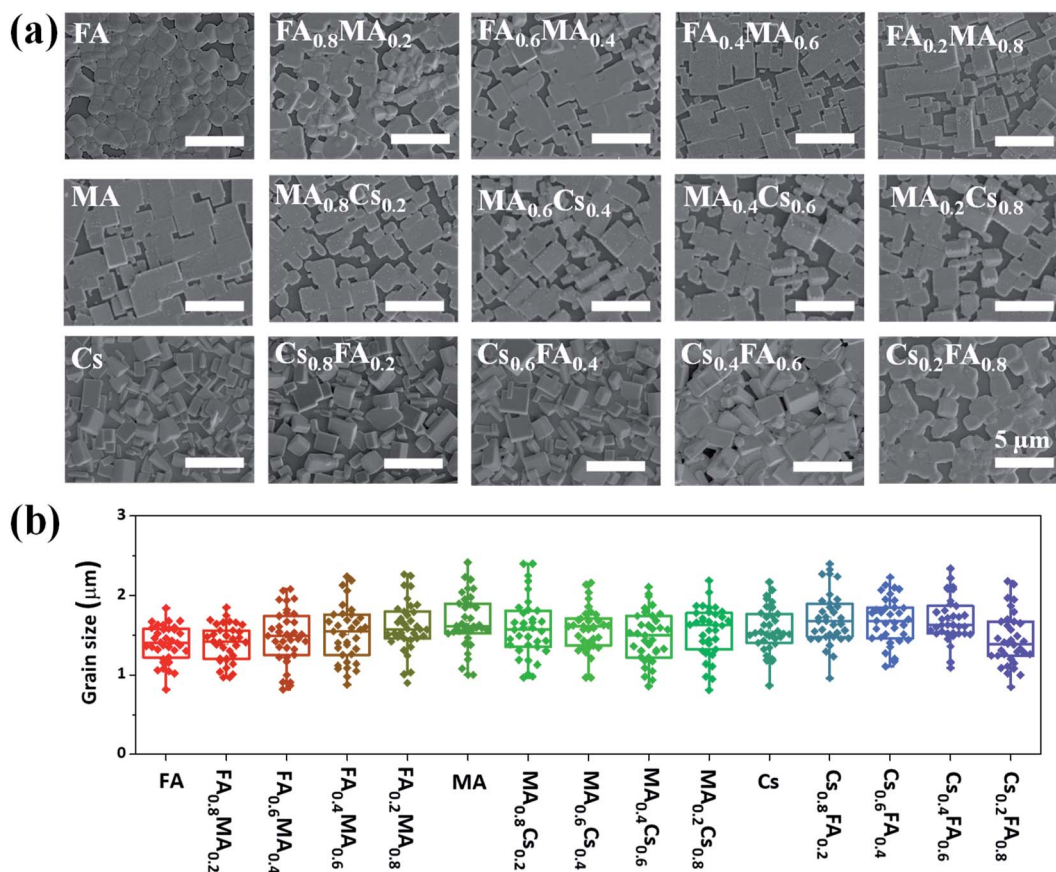

Fig. 3 (a) Top-view SEM images of inkjet-printed $FA_{1-x}MA_xPbBr_3$, $MA_{1-x}Cs_xPbBr_3$ and $Cs_{1-x}FA_xPbBr_3$ thin films with $x = 0$, 0.2, 0.4, 0.6, and 0.8, respectively. (b) Statistical distributions of the grain size of these inkjet-printed films.

reproducible and only took approximately eight minutes, highlighting the rapid production capacity of our inkjet printing technique.

Firstly, scanning electron microscopy (SEM) measurements are performed to investigate the morphology of the above inkjet-printed films, as displayed in Fig. 3a. Although some discontinuous regions exist in most printed films, dense crystalline grains still occupy most of the film surface. These printed films exhibit similar crystal sizes, and the average crystalline size of each film is in the vicinity of 1.5 μm according to the statistical analysis (Fig. 3b). Such a large average crystal size even exceeds that reported for spin-coated films[33,38] and can adequately express the basic optoelectronic properties of the corresponding films, and therefore these printed films are enough for the subsequent X-ray diffraction, absorption and PL characterization. More importantly, the very close grain size (Fig. 3b) for these films with different compositions enables us to generate an effective database with perovskite film properties for comparison given the fact that the perovskite grain size can greatly affect the optoelectronic properties of perovskite films, and this resulting database can vastly accelerate the discovery of novel perovskite materials for device applications.

To examine the crystal phase of these inkjet-printed films, X-ray diffraction (XRD) measurements are implemented. First of all, as shown in Fig. 4a, we compare the XRD patterns of three single-component films (namely $FAPbBr_3$, $MAPbBr_3$ and $CsPbBr_3$). Both $FAPbBr_3$ and $MAPbBr_3$ films exhibit two main diffraction peaks at the 2θ of ~15° and 30° corresponding to the (100) and (200) lattice planes, indicative of the formation of a cubic structure.[41,42] By contrast, an orthorhombic phase is formed in the $CsPbBr_3$ film given the fact that three dominant diffraction peaks at the 2θ of 15.5°, 21.8° and 30.9° can be assigned to (101), (121) and (202) planes, respectively.[43] With the increase of MA concentration in $FA_{1-x}MA_xPbBr_3$ from 0% to 100% (Fig. S4†), the (100) and (200) diffraction peaks are gradually shifted from 14.9° and 29.8° to 15.2° and 30.4°, respectively, indicating a decreased lattice spacing due to a gradual substitution of FA with smaller MA.[44] Additionally, a small amount of $PbBr_2$ indexed to the diffraction peak at ~12.5° is observed in the $FA_{1-x}MA_xPbBr_3$ system, and this phenomenon has been commonly reported in mixed perovskite films.[44–46] Similarly, the introduction of 0–100% smaller-sized Cs into $FAPbBr_3$ or $MAPbBr_3$ leads to a shrinkage of the interplanar spacing accompanied by a gradual shift of (100) and (200) main peaks towards slightly higher 2θ angles (Fig. S4†).[42,45,47] Meanwhile, the emergence of a characteristic peak located at ~11.8° means the formation of a parasitic $CsPb_2Br_5$ phase in $MA_{1-x}Cs_xPbBr_3$ and $Cs_{1-x}FA_xPbBr_3$, and such a secondary phase generally exists in the Cs-containing tribromide perovskite films according to previous studies.[48,49] When the Cs content surpasses 50%, the splitting of a single diffraction peak at ~30.5° into double peaks probably corresponds to a structural phase transition from the cubic to the orthorhombic structure. The above crystal phase analysis manifests that mixed perovskite films can be reliably manufactured by our high throughput approach.

The absorption and emission properties of these inkjet-printed films are analyzed via absorbance (Abs) and PL spectroscopy measurements. The absorption edges of $FA_{1-x}MA_x$-$PbBr_3$, $MA_{1-x}Cs_xPbBr_3$ and $Cs_{1-x}FA_xPbBr_3$ films are compared in Fig. S5,† and the corresponding optical bandgaps (E_g) extracted from Tauc plots (Fig. S6) are summarized in Table S2.† As expected, very close bandgap values of 2.2172, 2.2433 and 2.2915 eV are obtained for $FAPbBr_3$, $MAPbBr_3$ and $CsPbBr_3$ samples, respectively (Fig. 4b). Furthermore, the PL signals of $FAPbBr_3$, $MAPbBr_3$ and $CsPbBr_3$ films peak at 2.2574, 2.2916 and 2.3386 eV (Fig. 4c), respectively. For mixed film samples, their bandgaps range from 2.2172 to 2.2915 eV (Fig. 4d) and the
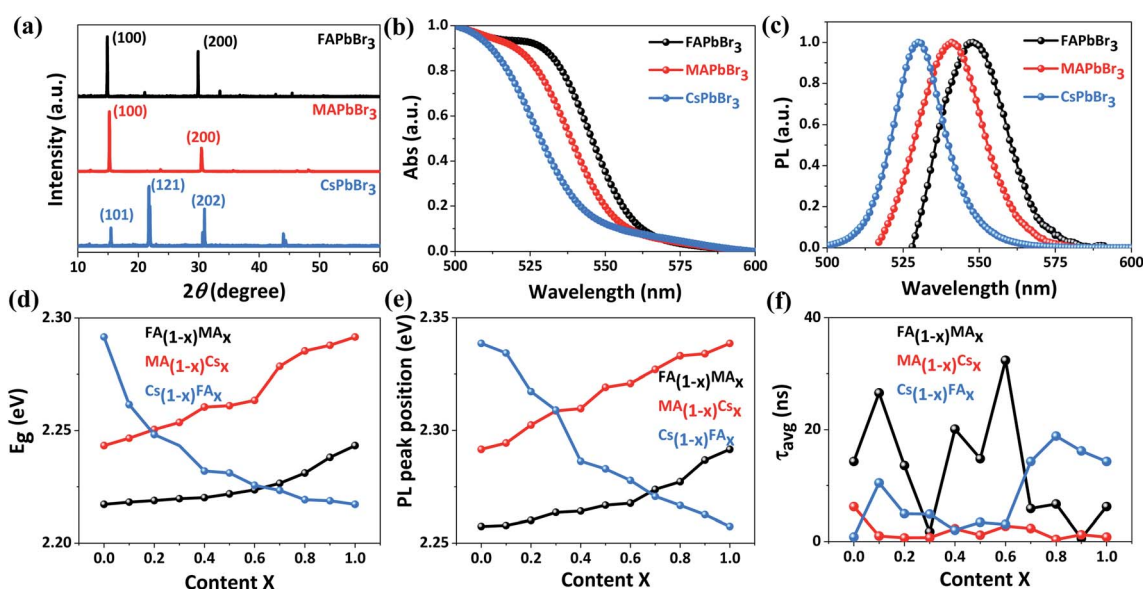

Fig. 4 XRD patterns (a), absorbance spectra (b) and PL spectra (c) of inkjet-printed $FAPbBr_3$, $MAPbBr_3$ and $CsPbBr_3$ thin films. Bandgaps (d), PL peak positions (e) and average PL lifetimes (τ_{avg}) (f) of inkjet-printed $FA_{1-x}MA_xPbBr_3$, $MA_{1-x}Cs_xPbBr_3$ and $Cs_{1-x}FA_xPbBr_3$ films as a function of x.

25506 | J. Mater. Chem. A, 2021, 9, 25502–25512

This journal is © The Royal Society of Chemistry 2021

corresponding PL peaks are located within 2.2574–2.3386 eV (Fig. 4e and S7†). The gradual change in the bandgap and PL peak position of these mixed samples is highly consistent with previous findings,[42,44,45,47] and also suggests an excellent miscibility of the as-prepared perovskite inks in our high throughput synthesis. This is further confirmed by energy-dispersive X-ray spectrometry (EDS) results (Table S3†), which show small deviations of <4% between the calculated and the experimentally measured Cs/Pb ratio.

To further quantitatively evaluate the charge transport behavior, time-resolved PL spectra of these printed films deposited on glass substrates are recorded and fitted to a biexponential decay (Fig. S8†), and the corresponding PL lifetimes are listed in Table S2.† In this case, the bimolecular recombination of long-lived free charges corresponds to the slow decay phase and the fast decay phase is ascribed to trapping into non-radiative trap states,[50] and thus we choose the average PL lifetime (τ_{avg}) of inkjet-printed films for comparison considering that both decay phases can impact the charge transfer dynamics. For each film, the most representative time-resolved PL spectrum close to average results is used in the calculation of PL lifetimes. As illustrated in Fig. 4f, these samples exhibit obviously different τ_{avg} in the range of 0.38–32.36 ns. It should be noted that a longer PL lifetime signifies a lower charge recombination rate and more efficient charge transport, which is very favorable for high-performance photovoltaic applications. In view of similar bandgaps (2.22–2.29 eV) for all film samples, the above average PL lifetime database allows us to efficiently screen these novel compositions and accelerate the discovery of novel tribromide perovskite materials for high-photovoltage and high-efficiency solar cells.

To exemplify the screening role of the PL lifetime database, two perovskite constituents are selected from the 30 tested mixed films to fabricate solar cells for device investigations.

Apparently, the $FA_{0.4}MA_{0.6}$ film exhibits the longest τ_{avg} of 32.36 ns out of the 30 samples, and the corresponding device based on $FA_{0.4}MA_{0.6}$ has great potential to yield a high V_{oc} and PCE. Meanwhile, six samples among the inkjet-printed films have a very short τ_{avg} of 0–1 ns, and these film candidates are all Cs-containing except the $FA_{0.1}MA_{0.9}$ sample. Considering that the Cs-containing tribromide perovskites usually suffer from a low solubility of CsBr in typically used deposition solvents and the resulting great difficulty in the direct adoption of commonly reported solution-processed deposition methods for fabricating high-quality thick films,[51] these Cs-containing compositions are excluded for device fabrication and comparison in this study. Consequently, we choose the $FA_{0.4}MA_{0.6}$ and $FA_{0.1}MA_{0.9}$ constituents as solar cell absorber materials and further compare the corresponding device performance. Since inkjet-printed $FA_{0.4}MA_{0.6}$ and $FA_{0.1}MA_{0.9}$ films with obvious discontinuous regions are not suitable for solar cell manufacture, the following discussion will focus on $FA_{0.4}MA_{0.6}$ and $FA_{0.1}MA_{0.9}$ based films and devices deposited by spin coating based on the fact that the spin coating technique normally produces high-performance perovskite solar cells.

Both $FA_{0.4}MA_{0.6}$ and $FA_{0.1}MA_{0.9}$ films have a uniform morphology with dense grains as shown in Fig. 5a and b, where the average grain size of the $FA_{0.4}MA_{0.6}$ film slightly surpasses that of the $FA_{0.1}MA_{0.9}$ counterpart on the basis of the statistical distribution (Fig. S9†). According to the cross-sectional SEM images, large columnar crystal grains form in both films and the film thickness is measured to be approximately 380 nm. XRD results (Fig. S10†) confirm the formation of a cubic structure in both films.[41] The $FA_{0.4}MA_{0.6}$ and $FA_{0.1}MA_{0.9}$ films show a bandgap of 2.23 and 2.25 eV according to Tauc plots (Fig. S11†) derived from ultraviolet-visible spectroscopy (Fig. 5c and d), respectively, and the corresponding PL peak are also located at 2.23 and 2.25 eV. The obtained bandgaps and PL peak
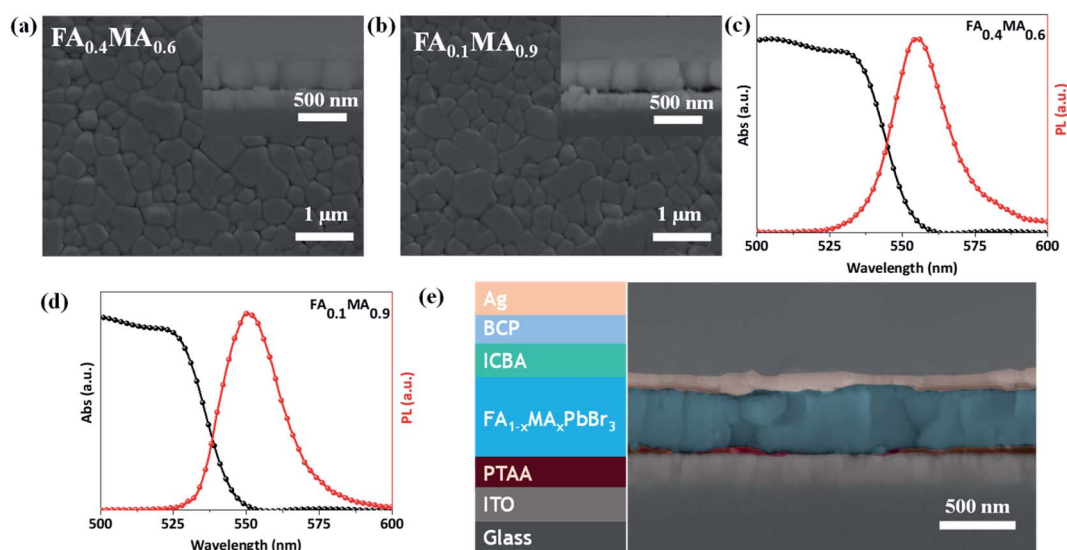

Fig. 5 Top-view and cross-sectional SEM images of spin-coated $FA_{0.4}MA_{0.6}$ (a) and $FA_{0.1}MA_{0.9}$ (b) films, respectively. Steady-state PL spectra and absorbance spectra of spin-coated $FA_{0.4}MA_{0.6}$ (c) and $FA_{0.1}MA_{0.9}$ (d) films, respectively. (e) Cross-sectional SEM image of a typical cell with a structure of ITO/PTAA/perovskite/ICBA/BCP/Ag.

locations of both films deposited by spin coating are very close to the corresponding values acquired for inkjet-printed films, further emphasizing the feasibility of our high throughput synthesis.

Subsequently, we estimate the photovoltaic performance of $FA_{0.4}MA_{0.6}$ and $FA_{0.1}MA_{0.9}$ based devices with an architecture of indium tin oxide (ITO)/poly(bis(4-phenyl)(2,4,6-trimethylphenyl)amine) (PTAA, 20 nm)/perovskite (380 nm)/indene-C_{60} bisadduct (ICBA, 50 nm)/bathocuproine (BCP, 8 nm)/Ag (100 nm), as depicted in Fig. 5e. Fig. 6a lists the energy levels of $MAPbBr_3$ and selected transport layers as previously reported.[52,53] The current density–voltage (J–V) curves of the champion devices measured under standard AM 1.5 G illumination conditions are shown in Fig. 6b, and the corresponding photovoltaic parameters and statistical distributions are summarized in Table 1. The $FA_{0.1}MA_{0.9}$ based champion device exhibits a short-circuit current density (J_{sc}) of 6.40 mA cm^{-2}, a V_{oc} of 1.45 V, and a fill factor (FF) of 71.4%, yielding a PCE of 6.62%. By contrast, much better photovoltaic parameters are achieved for the $FA_{0.4}MA_{0.6}$ champion device, with J_{sc} = 7.90 mA cm^{-2}, V_{oc} = 1.60 V, FF = 73.2% and PCE = 9.25%, showing a stabilized efficiency of 9.25% at the maximum power output point (Fig. S12†). Such an impressive PCE is among the highest reported efficiencies for tribromide perovskite solar cells.[36–40] The remarkably increased J_{sc} in the $FA_{0.4}MA_{0.6}$ cell in contrast with the $FA_{0.1}MA_{0.9}$ counterpart can be mainly attributed to more efficient charge collection (details in Fig. 7b). To better comprehend the enhancements in V_{oc} and FF in the $FA_{0.4}MA_{0.6}$ device, the series resistance (R_s) and the dark saturated current density (J_0) are calculated using the classical diode equation:

$$J = J_{sc} - J_0\left[\exp\left(\frac{q(V + JR_s)}{nkT}\right) - 1\right] \quad (1)$$

where n denotes the ideality factor, kT/q represents the thermal voltage, J is the device output current density, and V stands for the applied voltage. The corresponding calculation details are described in the ESI.† The plots of $-dV/dJ$ versus $(J_{sc} - J)^{-1}$ and $\ln(J_{sc} - J)$ versus $(V + R_sJ)$ for both devices are illustrated in Fig. 6c and d. The R_s for the $FA_{0.4}MA_{0.6}$ device is estimated to be 2.48 Ω cm^{-2}, lower than the corresponding value (3.08 Ω cm^{-2}) obtained for the $FA_{0.1}MA_{0.9}$ counterpart. The reduced R_s can partially explain a slightly higher FF in the $FA_{0.4}MA_{0.6}$ cell.[54] Moreover, the J_0 for the $FA_{0.4}MA_{0.6}$ device is calculated to be 6.6 × 10^{-7} mA cm^{-2}, which is much smaller than that (9.7 × 10^{-7} mA cm^{-2}) for the $FA_{0.1}MA_{0.9}$ counterpart. The recombination rate is directly correlated with J_0 based on the fact that J_0 is a parameter signifying the thermal emission rate of electrons from the valence band to the conduction band. The smaller J_0 in the $FA_{0.4}MA_{0.6}$ device manifests a lower recombination loss, and accordingly a higher V_{oc}.[55,56] The superior device performance (especially V_{oc}) of the $FA_{0.4}MA_{0.6}$ cell to the $FA_{0.1}MA_{0.9}$ counterpart well supports the screening protocol based on the above-mentioned PL lifetime database, highlighting the advantage of accelerated discovery of novel perovskite materials via our screening approach.

It is worth noting that both $FA_{0.4}MA_{0.6}$ and $FA_{0.1}MA_{0.9}$ devices have no obvious hysteresis of J–V characteristics with respect to the voltage scan directions (Fig. S13†). The J_{sc} values obtained from J–V curves are in accordance with those integrated from external quantum efficiency (EQE) spectra (Fig. 6e). Moreover, photothermal deflection spectroscopy (PDS) measurements are carried out to analyze the defects within the sub-bandgap region of both films. Evidently, the sub-bandgap absorption coefficient (α) below 2.2 eV of the $FA_{0.1}MA_{0.9}$ film is much larger than that of the $FA_{0.4}MA_{0.6}$ counterpart (Fig. 6f), implying a significant reduction of trap states in the $FA_{0.4}MA_{0.6}$
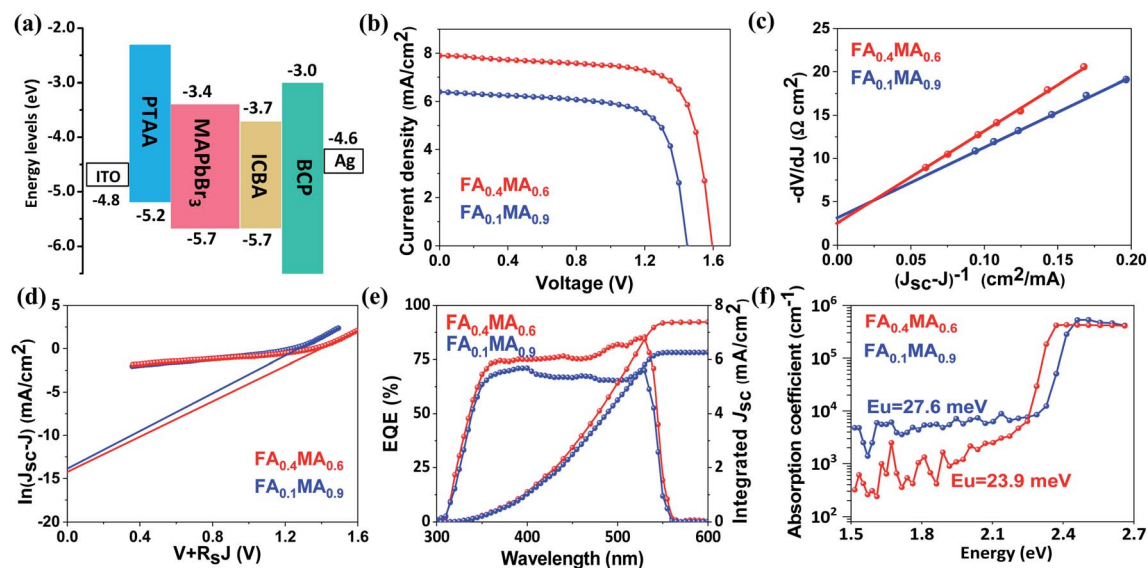

Fig. 6 (a) The energy diagram of each layer in the device, and the energy levels of PTAA, $MAPbBr_3$ and ICBA were obtained from previous studies.[52,53] (b) J–V characteristics of $FA_{0.4}MA_{0.6}$ and $FA_{0.1}MA_{0.9}$ based champion solar cells under AM 1.5 G solar irradiation, where a reverse scan from 1.65 to −0.1 V is performed with a scan rate of 0.1 V s^{-1}. Plots of $-dV/dJ$ versus $(J_{sc} - J)^{-1}$ (c) and $\ln(J_{sc} - J)$ versus $(V + R_sJ)$ (d) as well as their linear fitting, and both fitting curves are situated around the corresponding V_{oc}. (e) EQE spectra and integrated J_{sc}. (f) PDS absorbance spectra of $FA_{0.4}MA_{0.6}$ and $FA_{0.1}MA_{0.9}$ films coated on quartz substrates.

25508 | J. Mater. Chem. A, 2021, 9, 25502–25512

This journal is © The Royal Society of Chemistry 2021

Table 1 Summary of the photovoltaic parameters of $FA_{0.4}MA_{0.6}$ and $FA_{0.1}MA_{0.9}$ based solar cells

Active layer	J_{sc} [mA cm^{-2}]	V_{oc} [V]	FF [%]	PCE [%]
$FA_{0.4}MA_{0.6}$	7.90[a]	1.60	73.2	9.25
	7.71 ± 0.2[b]	1.58 ± 0.02	71.6 ± 1.5	8.72 ± 0.5
$FA_{0.1}MA_{0.9}$	6.40	1.45	71.4	6.62
	6.18 ± 0.3	1.41 ± 0.04	69.5 ± 2.0	6.06 ± 0.6

[a] The value from the champion devices. [b] The average value from 20 cells.

Table 2 Parameters used in the calculation of non-radiative recombination losses. J_{sc} and V_{oc} are taken from J–V curves. $J_{0,rad}$ and $V_{oc,rad}$ are calculated based on highly sensitive EQE spectra and ΔV_{oc} from $V_{oc,rad} - V_{oc}$

Active layer	$FA_{0.4}MA_{0.6}$	$FA_{0.1}MA_{0.9}$
J_{sc} [mA cm^{-2}]	7.90	6.40
$J_{0,rad}$ [mA cm^{-2}]	1.6×10^{-33}	9.3×10^{-34}
$V_{oc,rad}$ [V]	2.01	2.01
V_{oc} [V] measured	1.60	1.45
ΔV_{oc} [V] ($V_{oc,rad} - V_{oc}$)	0.41	0.56

film in comparison with the $FA_{0.1}MA_{0.9}$ film, which benefits the suppression of non-radiative charge recombination. Besides, the electronic disorder of perovskite films can be quantified by the Urbach energy (E_u), which is computed by a single-exponential fit to the PDS spectra at the absorption edge. As a result, the $FA_{0.4}MA_{0.6}$ film has a much lower E_u (23.9 meV) compared with the $FA_{0.1}MA_{0.9}$ counterpart (27.6 meV), indicative of a lower level of energetic disorder existing in the $FA_{0.4}MA_{0.6}$ film.[57,58] Such a lower level of energetic disorder enables a reduction of the parasitic charge recombination, consistent with the declining J_0 observed above in the $FA_{0.4}MA_{0.6}$ device.

To demonstrate the V_{oc} reproducibility, V_{oc} statistical distributions from 20 cells are also presented in Table 1. The $FA_{0.1}MA_{0.9}$ device exhibits an average V_{oc} of 1.41 V with a maximum value of 1.45 V. In contrast, the maximum V_{oc} reaches 1.60 V in the $FA_{0.4}MA_{0.6}$ cell with an average value of 1.58 V, which is among the highest reported V_{oc} values for tribromide perovskite devices (Table S4†). In addition, we further explore the radiative limit of V_{oc} ($V_{oc,rad}$, namely the V_{oc} limit) for

both devices and the corresponding non-radiative recombination losses (ΔV_{oc}), which can be determined from eqn (2) and (3), respectively. Here, J_{sc} denotes the measured short-circuit current density under one sun illumination, and $J_{0,rad}$ is the saturation current density for radiative recombination. The $V_{oc,rad}$ can be obtained when the absorbed photon flux is balanced exactly by the emitted flux under open-circuit conditions. As shown in Fig. 7a, the highly sensitive EQE spectra of both devices are derived from normalized PDS spectra (Fig. S14†) and can be adopted to compute $J_{0,rad}$, where the electroluminescence spectra extend the absorption edge into the low-energy region to ensure calculation with sufficiently high resolution (details in the ESI†).[59,60] The measured and calculated parameters used for the analysis of non-radiative recombination losses are summarized in Table 2. Amazingly, the $V_{oc,rad}$ obtained is as high as 2.01 V for both $FA_{0.1}MA_{0.9}$ and $FA_{0.4}MA_{0.6}$ devices, much higher than the value (1.30–1.33 V) acquired for triiodide perovskite solar cells.[61,62] This $V_{oc,rad}$ value is also consistent with that (1.95 V) reported for a MAPbBr$_3$ solar
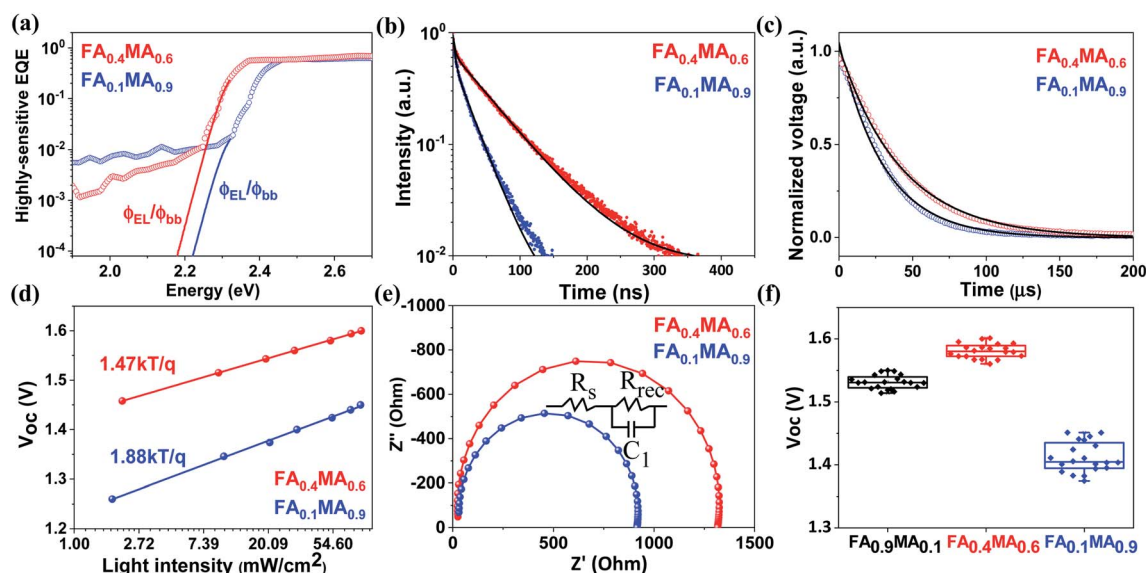

Fig. 7 (a) Highly sensitive EQE spectra (dotted line) derived from normalized PDS spectra in Fig. S14,† where the absorption edge is extended by the ratio of the emitted photon flux from electroluminescence to the photon flux for blackbody radiation (solid line). (b) Time-resolved PL spectra of $FA_{0.4}MA_{0.6}$ and $FA_{0.1}MA_{0.9}$ films coated on glass substrates. Normalized TPV decay (c), light intensity dependent V_{oc} (d), and Nyquist plots (e) of $FA_{0.4}MA_{0.6}$ and $FA_{0.1}MA_{0.9}$ based solar cells, respectively. (f) V_{oc} statistical distributions of $FA_{0.9}MA_{0.1}$, $FA_{0.4}MA_{0.6}$ and $FA_{0.1}MA_{0.9}$ based devices from 20 cells.

This journal is © The Royal Society of Chemistry 2021

J. Mater. Chem. A, 2021, **9**, 25502–25512 | **25509**

cell in our previous work.[33] Accordingly, the $FA_{0.1}MA_{0.9}$ and $FA_{0.4}MA_{0.6}$ devices deliver a ΔV_{oc} value of 0.56 and 0.41 V, respectively, suggesting a much lower level of non-radiative recombination losses existing in the $FA_{0.4}MA_{0.6}$ stack. Evidently, these tribromide devices suffer more from non-radiative recombination losses than their triiodide analogues which were reported with ΔV_{oc} values of 0.1–0.2 V.[59,63] This comparison also means that the V_{oc} for these devices may be further increased if non-radiative recombination can be remarkably suppressed even further.

$$V_{oc,rad} = \frac{kT}{q} \ln\left(\frac{J_{sc}}{J_{0,rad}} + 1\right) \qquad (2)$$

$$\Delta V_{oc} = V_{oc,rad} - V_{oc} \qquad (3)$$

In order to further comprehend the distinction in device performance, the charge transport characteristics are explored *via* recording the time-resolved PL spectra of both films deposited on glass substrates, as displayed in Fig. 7b. A bi-exponential fitting to the time-resolved PL spectra gives the corresponding PL lifetimes (Table S5†). The $FA_{0.1}MA_{0.9}$ film shows an average PL lifetime of 13.5 ns, while a much longer average PL lifetime (37.3 ns) is achieved in the case of the $FA_{0.4}MA_{0.6}$ film, in agreement with trends observed in the PL lifetime database for inkjet-printed films. The extension of PL lifetimes in the $FA_{0.4}MA_{0.6}$ film means better charge transport to a large extent, contributing to a higher photocurrent in devices. Additionally, transient photovoltage (TPV) measurements are conducted to determine the charge recombination lifetime of both devices, as illustrated in Fig. 7c. The normalized photo-voltage of the $FA_{0.4}MA_{0.6}$ device decays with a long lifetime of 42.2 μs, which is almost 1.5 times that (30.4 μs) of the $FA_{0.1}MA_{0.9}$ counterpart, indicating lower charge recombination losses in the $FA_{0.4}MA_{0.6}$ cell.[64,65]

To gain further insight into the relationship between charge recombination and device performance with different absorber layers, the charge recombination mechanism is evaluated on the basis of light intensity dependent V_{oc} and electrochemical imped-ance spectroscopy (EIS). Normally, the slope of V_{oc} *versus* the natural logarithm of light intensity deviating from kT/q manifests the existence of trap-assisted charge recombination.[66–68] As depic-ted in Fig. 7d, the corresponding slope for $FA_{0.1}MA_{0.9}$ and $FA_{0.4}MA_{0.6}$ devices is determined to be $1.88kT/q$ and $1.47kT/q$, respectively. The smaller slope for the $FA_{0.4}MA_{0.6}$ device suggests a more effective suppression of charge recombination through trap states, in good accordance with the decreased defects in the $FA_{0.4}MA_{0.6}$ film, thus leading to a higher V_{oc}. Fig. 7e presents the Nyquist plots from impedance spectra of both devices and the corresponding circuit model. The $FA_{0.4}MA_{0.6}$ device has a much larger recombination resistance (R_{rec}) (1285 Ω) than the $FA_{0.1}MA_{0.9}$ counterpart (879 Ω), suggesting that the charge recombination process can be more effectively suppressed in the $FA_{0.4}MA_{0.6}$ device.[69,70] In general, substantially decreased charge recombination losses exist in the $FA_{0.4}MA_{0.6}$ device in comparison with the $FA_{0.1}MA_{0.9}$ counterpart on the basis of TPV and light intensity

dependent V_{oc} as well as EIS results, which inevitably contribute to its better device performance.

In order to further confirm the validity of the above PL lifetime database for novel composition screening, we employ another new composition ($FA_{0.9}MA_{0.1}$) as an example to check the achievable V_{oc}, given the fact that the average PL lifetime of the $FA_{0.9}MA_{0.1}$ film is ranked second (26.58 ns) among all inkjet-printed samples. According to the statistical analysis from 20 cells, the $FA_{0.9}MA_{0.1}$ device yields a V_{oc} of 1.53 ± 0.02 V with a maximum value of 1.55 V (Fig. 7f). These V_{oc} values are slightly smaller than that (1.58 ± 0.02) of the $FA_{0.4}MA_{0.6}$ device, but obviously outperform that (1.41 ± 0.04) obtained for the $FA_{0.1}MA_{0.9}$ counterpart. This result further supports that our PL lifetime database can indeed screen out novel tribromide perovskites for high-photovoltage solar cells. With this we conclude that our proposed composition screening protocol based on high throughput inkjet printing can effectively accelerate the discovery of novel perovskite materials for device applications.

3 Conclusion

In summary, we have developed a highly efficient composition screening protocol based on high throughput inkjet printing of discontinuous rather than compact perovskite films with representative and comparable properties to accelerate the discovery of novel tribromide perovskites for high-photovoltage solar cells. Specifically, the sequential inkjet printing of three precursor solutions yields 30 mixed tribromide perovskite films with similar bandgaps rapidly and automatically, where the good control of the crystallization behaviour produces a very close grain size for all samples. Thus, the corresponding PL lifetime database enables us to efficiently screen and identify novel compositions for high-photovoltage solar cells. To verify this, two constituents of $FA_{0.4}MA_{0.6}$ and $FA_{0.1}MA_{0.9}$ with a long (32.36 ns) and short (0.57 ns) average PL lifetime, respectively, are selected out of the 30 tested films as device analysis. As anticipated, the $FA_{0.4}MA_{0.6}$ device achieves a high V_{oc} of 1.60 V along with a peak PCE of 9.25%, which greatly outperform those (1.45 V and 6.62%) acquired for the $FA_{0.1}MA_{0.9}$ counterpart. The as-obtained V_{oc} of 1.60 V is among the highest reported V_{oc} values for tribromide perovskite devices, and more importantly, the $V_{oc,rad}$ is estimated to be as high as 2.01 V for both devices for the first time. The greatly enhanced device performance (especially V_{oc}) can be mainly attributed to the reduced trap states, lower level of energetic disorder and more efficient charge transport as well as considerably decreased charge recombination losses. In addition, the validity of the PL lifetime database is further confirmed by a high V_{oc} of 1.55 V achieved in devices based on another novel $FA_{0.9}MA_{0.1}$ composition with a long average PL lifetime. These results highlight that our proposed high throughput composition screening approach can effectively and efficiently accelerate the discovery of novel perovskites for advanced device applications.

Author contributions

X. Z. W., S. H. Y., and B. M. X. designed and directed the study. S. C. and L. H. Z. conceived and performed the film and device

fabrication work. Z. Q. Z. and S. K. S. performed the PDS measurements. Y. L. L. and Y. L. conducted the PL measurements. W. Z. C. and H. Y. L. contributed to the TPV measurements and analysis. Q. L. L. and B. Z. carried out the SEM measurements. Y. C. Q., T. Y., and J. R. conducted the XRD and absorbance measurements. S. M. C., X. D. X., and S. Y. D. provided advice and expertise. S. C. and B. M. X. wrote the original draft of the manuscript, and all authors contributed to the discussion.

Conflicts of interest

The authors declare no competing financial interest.

References

1 N. J. Jeon, J. H. Noh, W. S. Yang, Y. C. Kim, S. Ryu, J. Seo and S. I. Seok, *Nature*, 2015, **517**, 476–480.

2 M. Liu, M. B. Johnston and H. J. Snaith, *Nature*, 2013, **501**, 395–398.

3 N. J. Jeon, J. H. Noh, Y. C. Kim, W. S. Yang, S. Ryu and S. I. Seok, *Nat. Mater.*, 2014, **13**, 897–903.

4 Q. Jiang, Y. Zhao, X. Zhang, X. Yang, Y. Chen, Z. Chu, Q. Ye, X. Li, Z. Yin and J. You, *Nat. Photonics*, 2019, **13**, 460–466.

5 H. Min, M. Kim, S.-U. Lee, H. Kim, G. Kim, K. Choi, J. H. Lee and S. I. Seok, *Science*, 2019, **366**, 749–753.

6 E. H. Jung, N. J. Jeon, E. Y. Park, C. S. Moon, T. J. Shin, T.-Y. Yang, J. H. Noh and J. Seo, *Nature*, 2019, **567**, 511–515.

7 M. Kim, G.-H. Kim, T. K. Lee, I. W. Choi, H. W. Choi, Y. Jo, Y. J. Yoon, J. W. Kim, J. Lee, D. Huh, H. Lee, S. K. Kwak, J. Y. Kim and D. S. Kim, *Joule*, 2019, **3**, 2179–2192.

8 J. J. Yoo, S. Wieghold, M. C. Sponseller, M. R. Chua, S. N. Bertram, N. T. P. Hartono, J. S. Tresback, E. C. Hansen, J.-P. Correa-Baena, V. Bulović, T. Buonassisi, S. S. Shin and M. G. Bawendi, *Energy Environ. Sci.*, 2019, **12**, 2192–2199.

9 J. Kirman, A. Johnston, D. A. Kuntz, M. Askerka, Y. Gao, P. Todorović, D. Ma, G. G. Privé and E. H. Sargent, *Matter*, 2020, **2**, 938–947.

10 S. Chen, Y. Hou, H. Chen, X. Tang, S. Langner, N. Li, T. Stubhan, I. Levchuk, E. Gu, A. Osvet and C. J. Brabec, *Adv. Energy Mater.*, 2018, **8**, 1701543.

11 S. Sun, N. T. P. Hartono, Z. D. Ren, F. Oviedo, A. M. Buscemi, M. Layurova, D. X. Chen, T. Ogunfunmi, J. Thapa, S. Ramasamy, C. Settens, B. L. DeCost, A. G. Kusne, Z. Liu, S. I. P. Tian, I. M. Peters, J.-P. Correa-Baena and T. Buonassisi, *Joule*, 2019, **3**, 1437–1451.

12 S. Chen, L. Zhang, L. Yan, X. Xiang, X. Zhao, S. Yang and B. Xu, *Adv. Funct. Mater.*, 2019, **29**, 1905487.

13 W. Nie, H. Tsai, R. Asadpour, J.-C. Blancon, A. J. Neukirch, G. Gupta, J. J. Crochet, M. Chhowalla, S. Tretiak, M. A. Alam, H.-L. Wang and A. D. Mohite, *Science*, 2015, **347**, 522–525.

14 F. Guo, S. Qiu, J. Hu, H. Wang, B. Cai, J. Li, X. Yuan, X. Liu, K. Forberich, C. J. Brabec and Y. Mai, *Adv. Sci.*, 2019, **6**, 1901067.

15 F. Guo, W. He, S. Qiu, C. Wang, X. Liu, K. Forberich, C. J. Brabec and Y. Mai, *Adv. Funct. Mater.*, 2019, **29**, 1900964.

16 C. Li, Y. Pan, J. Hu, S. Qiu, C. Zhang, Y. Yang, S. Chen, X. Liu, C. J. Brabec, M. K. Nazeeruddin, Y. Mai and F. Guo, *ACS Energy Lett.*, 2020, **5**, 1386–1395.

17 W.-Q. Wu, Q. Wang, Y. Fang, Y. Shao, S. Tang, Y. Deng, H. Lu, Y. Liu, T. Li, Z. Yang, A. Gruverman and J. Huang, *Nat. Commun.*, 2018, **9**, 1625.

18 J. G. Tait, S. Manghooli, W. Qiu, L. Rakocevic, L. Kootstra, M. Jaysankar, C. A. Masse de la Huerta, U. W. Paetzold, R. Gehlhaar, D. Cheyns, P. Heremans and J. Poortmans, *J. Mater. Chem. A*, 2016, **4**, 3792–3797.

19 M. Park, W. Cho, G. Lee, S. C. Hong, M.-c. Kim, J. Yoon, N. Ahn and M. Choi, *Small*, 2019, **15**, 1804005.

20 M. Bag, Z. Jiang, L. A. Renna, S. P. Jeong, V. M. Rotello and D. Venkataraman, *Mater. Lett.*, 2016, **164**, 472–475.

21 X. Peng, J. Yuan, S. Shen, M. Gao, A. S. R. Chesman, H. Yin, J. Cheng, Q. Zhang and D. Angmo, *Adv. Funct. Mater.*, 2017, **27**, 1703704.

22 C. Liang, P. Li, H. Gu, Y. Zhang, F. Li, Y. Song, G. Shao, N. Mathews and G. Xing, *Sol. RRL*, 2018, **2**, 1700217.

23 A. J. Huckaba, Y. Lee, R. Xia, S. Paek, V. C. Bassetto, E. Oveisi, A. Lesch, S. Kinge, P. J. Dyson, H. Girault and M. K. Nazeeruddin, *Energy Technol.*, 2019, **7**, 317–324.

24 H. Eggers, F. Schackmar, T. Abzieher, Q. Sun, U. Lemmer, Y. Vaynzof, B. S. Richards, G. Hernandez-Sosa and U. W. Paetzold, *Adv. Energy Mater.*, 2020, **10**, 1903184.

25 S.-G. Li, K.-J. Jiang, M.-J. Su, X.-P. Cui, J.-H. Huang, Q.-Q. Zhang, X.-Q. Zhou, L.-M. Yang and Y.-L. Song, *J. Mater. Chem. A*, 2015, **3**, 9092–9097.

26 J. H. Heo and S. H. Im, *Adv. Mater.*, 2015, **28**, 5121–5125.

27 J. Luo, J.-H. Im, M. T. Mayer, M. Schreier, M. K. Nazeeruddin, N.-G. Park, S. D. Tilley, H. J. Fan and M. Grätzel, *Science*, 2014, **345**, 1593–1596.

28 M. Schreier, L. Curvat, F. Giordano, L. Steier, A. Abate, S. M. Zakeeruddin, J. Luo, M. T. Mayer and M. Grätzel, *Nat. Commun.*, 2015, **6**, 7326.

29 C. Zhang, Y.-N. Lu, W.-Q. Wu and L. Wang, *Nano Energy*, 2021, **81**, 105634.

This journal is © The Royal Society of Chemistry 2021

J. Mater. Chem. A, 2021, **9**, 25502–25512 | **25511**

30 W. Feng, C. Zhang, J.-X. Zhong, L. Ding and W.-Q. Wu, *Chem. Commun.*, 2020, **56**, 5006–5009.

31 J.-X. Zhong, J.-F. Liao, Y. Jiang, L. Wang, D.-B. Kuang and W.-Q. Wu, *J. Mater. Chem. A*, 2020, **8**, 9743–9752.

32 N. Arora, S. Orlandi, M. I. Dar, S. Aghazada, G. Jacopin, M. Cavazzini, E. Mosconi, P. Gratia, F. De Angelis, G. Pozzi, M. Graetzel and M. K. Nazeeruddin, *ACS Energy Lett.*, 2016, **1**, 107–112.

33 S. Chen, Y. Hou, H. Chen, M. Richter, F. Guo, S. Kahmann, X. Tang, T. Stubhan, H. Zhang, N. Li, N. Gasparini, C. O. R. Quiroz, L. S. Khanzada, G. J. Matt, A. Osvet and C. J. Brabec, *Adv. Energy Mater.*, 2016, **6**, 1600132.

34 C. Zuo and L. Ding, *Adv. Energy Mater.*, 2017, **7**, 1601193.

35 C.-G. Wu, C.-H. Chiang and S. H. Chang, *Nanoscale*, 2016, **8**, 4077–4085.

36 N. K. Noel, B. Wenger, S. N. Habisreutinger, J. B. Patel, T. Crothers, Z. Wang, R. J. Nicholas, M. B. Johnston, L. M. Herz and H. J. Snaith, *ACS Energy Lett.*, 2018, **3**, 1233–1240.

37 J. H. Heo, D. H. Song and S. H. Im, *Adv. Mater.*, 2014, **26**, 8179–8183.

38 Y. Liang, Y. Wang, C. Mu, S. Wang, X. Wang, D. Xu and L. Sun, *Adv. Energy Mater.*, 2018, **8**, 1701159.

39 J. Duan, Y. Zhao, X. Yang, Y. Wang, B. He and Q. Tang, *Adv. Energy Mater.*, 2018, **8**, 1802346.

40 X. Hu, X.-F. Jiang, X. Xing, L. Nian, X. Liu, R. Huang, K. Wang, H.-L. Yip and G. Zhou, *Sol. RRL*, 2018, **2**, 1800083.

41 A. Kojima, K. Teshima, Y. Shirai and T. Miyasaka, *J. Am. Chem. Soc.*, 2009, **131**, 6050–6051.

42 X. Zhang, H. Liu, W. Wang, J. Zhang, B. Xu, K. L. Karen, Y. Zheng, S. Liu, S. Chen, K. Wang and X. W. Sun, *Adv. Mater.*, 2017, **29**, 1606405.

43 H. Cho, C. Wolf, J. S. Kim, H. J. Yun, J. S. Bae, H. Kim, J.-M. Heo, S. Ahn and T.-W. Lee, *Adv. Mater.*, 2017, **29**, 1700579.

44 B. Slimi, M. Mollar, B. Marí and R. Chtourou, *J. Electron. Mater.*, 2019, **48**, 8014–8023.

45 H. Cho, J. S. Kim, C. Wolf, Y.-H. Kim, H. J. Yun, S.-H. Jeong, A. Sadhanala, V. Venugopalan, J. W. Choi, C.-L. Lee, R. H. Friend and T.-W. Lee, *ACS Nano*, 2018, **12**, 2883–2892.

46 C. Yi, J. Luo, S. Meloni, A. Boziki, N. Ashari-Astani, C. Grätzel, S. M. Zakeeruddin, U. Röthlisberger and M. Grätzel, *Energy Environ. Sci.*, 2016, **9**, 656–662.

47 A. A. Sutanto, V. I. E. Queloz, I. Garcia-Benito, K. Laasonen, B. Smit, M. K. Nazeeruddin, O. A. Syzgantseva and G. Grancini, *APL Mater.*, 2019, **7**, 041110.

48 C. Tenailleau, S. Aharon, B.-E. Cohen and L. Etgar, *Nanoscale Adv.*, 2019, **1**, 147–153.

49 G. Tong, M. Jiang, D.-Y. Son, L. Qiu, Z. Liu, L. K. Ono and Y. Qi, *ACS Appl. Mater. Interfaces*, 2020, **12**, 14185–14194.

50 Y. Yamada, T. Yamada, A. Shimazaki, A. Wakamiya and Y. Kanemitsu, *J. Phys. Chem. Lett.*, 2016, **7**, 1972–1977.

51 J. B. Hoffman, G. Zaiats, I. Wappes and P. V. Kamat, *Chem. Mater.*, 2017, **29**, 9767–9774.

52 Y. He, H.-Y. Chen, J. Hou and Y. Li, *J. Am. Chem. Soc.*, 2010, **132**, 1377–1382.

53 S. Ryu, J. H. Noh, N. J. Jeon, Y. Chan Kim, W. S. Yang, J. Seo and S. I. Seok, *Energy Environ. Sci.*, 2014, **7**, 2614–2618.

54 W. Kong, W. Li, C. Liu, H. Liu, J. Miao, W. Wang, S. Chen, M. Hu, D. Li, A. Amini, S. Yang, J. Wang, B. Xu and C. Cheng, *ACS Nano*, 2019, **13**, 1625–1634.

55 S. Chen, N. Shen, L. Zhang, L. Zhang, S. H. Cheung, S. Chen, S. K. So and B. Xu, *Adv. Funct. Mater.*, 2020, **30**, 1907759.

56 J. You, Y. Yang, Z. Hong, T.-B. Song, L. Meng, Y. Liu, C. Jiang, H. Zhou, W.-H. Chang, G. Li and Y. Yang, *Appl. Phys. Lett.*, 2014, **105**, 183902.

57 X. Meng, J. Zhou, J. Hou, X. Tao, S. H. Cheung, S. K. So and S. Yang, *Adv. Mater.*, 2018, **30**, 1706975.

58 A. Ng, Z. Ren, H. Hu, P. W. K. Fong, Q. Shen, S. H. Cheung, P. Qin, J.-W. Lee, A. B. Djurišić, S. K. So, G. Li, Y. Yang and C. Surya, *Adv. Mater.*, 2018, **30**, 1804402.

59 D. Luo, W. Yang, Z. Wang, A. Sadhanala, Q. Hu, R. Su, R. Shivanna, G. F. Trindade, J. F. Watts, Z. Xu, T. Liu, K. Chen, F. Ye, P. Wu, L. Zhao, J. Wu, Y. Tu, Y. Zhang, X. Yang, W. Zhang, R. H. Friend, Q. Gong, H. J. Snaith and R. Zhu, *Science*, 2018, **360**, 1442–1446.

60 T. Kirchartz and U. Rau, *J. Appl. Phys.*, 2007, **102**, 104510.

61 W. Tress, N. Marinova, O. Inganäs, M. K. Nazeeruddin, S. M. Zakeeruddin and M. Graetzel, *Adv. Energy Mater.*, 2015, **5**, 1400812.

62 K. Tvingstedt, O. Malinkiewicz, A. Baumann, C. Deibel, H. J. Snaith, V. Dyakonov and H. J. Bolink, *Sci. Rep.*, 2014, **4**, 6071.

63 M. Saliba, T. Matsui, K. Domanski, J.-Y. Seo, A. Ummadisingu, S. M. Zakeeruddin, J.-P. Correa-Baena, W. R. Tress, A. Abate, A. Hagfeldt and M. Grätzel, *Science*, 2016, **354**, 206–209.

64 J. Tian, Q. Xue, X. Tang, Y. Chen, N. Li, Z. Hu, T. Shi, X. Wang, F. Huang, C. J. Brabec, H.-L. Yip and Y. Cao, *Adv. Mater.*, 2019, **31**, 1901152.

65 W. Chen, Y. Wu, J. Fan, A. B. Djurišić, F. Liu, H. W. Tam, A. Ng, C. Surya, W. K. Chan, D. Wang and Z. B. He, *Adv. Energy Mater.*, 2018, **8**, 1703519.

66 S. Chen, N. Shen, L. Zhang, W. Kong, L. Zhang, C. Cheng and B. Xu, *J. Mater. Chem. A*, 2019, **7**, 9542–9549.

67 L. Yan, Q. Xue, M. Liu, Z. Zhu, J. Tian, Z. Li, Z. Chen, Z. Chen, H. Yan, H.-L. Yip and Y. Cao, *Adv. Mater.*, 2018, **30**, 1802509.

68 B. Zhao, M. Abdi-Jalebi, M. Tabachnyk, H. Glass, V. S. Kamboj, W. Nie, A. J. Pearson, Y. Puttisong, K. C. Gödel, H. E. Beere, D. A. Ritchie, A. D. Mohite, S. E. Dutton, R. H. Friend and A. Sadhanala, *Adv. Mater.*, 2017, **29**, 1604744.

69 S. Ahmad, P. Fu, S. Yu, Q. Yang, X. Liu, X. Wang, X. Wang, X. Guo and C. Li, *Joule*, 2019, **3**, 794–806.

70 J. Ma, G. Yang, M. Qin, X. Zheng, H. Lei, C. Chen, Z. Chen, Y. Guo, H. Han, X. Zhao and G. Fang, *Adv. Sci.*, 2017, **4**, 1700031.

25512 | *J. Mater. Chem. A*, 2021, **9**, 25502–25512

This journal is © The Royal Society of Chemistry 2021